SUPPLEMENTAL INFORMATION [SI] APPENDIX

1. SI TABLES & FIGURES

2. SI EXPERIMENTAL PROCEDURES

3. SI DISCUSSION

4. SI REFERENCES

SI TABLES & FIGURES

Table S1 | Clinical and Demographic Characteristics - Schizophrenia Sample (Combining Olin and COBRE)

Characteristic	HCS (N=164)		SCZ (N=161)		Significance	
	M	S.D.	M	S.D.	T Value / Chi-Square	P Value (two-tailed)
Age (in years)	33.02	12.04	35.23	12.76	1.61	0.11
Gender (% male)	67		76		1.87	0.06
Parental Education	4.66	1.76	4.24	1.95	2.01*	0.046
Participant's education	5.06	1.41	4.01	1.42	6.70*	<.0001
Handedness (% right)	92.07		83.85		2.29	0.2
Signal-to-noise (SNR)	214.47	63.01	203.57	77.39	1.39	0.2
% Frames Flagged	14.05	15.72	23.57	23.76	4.27*	<.0001
Medication (CPZ equivalents)	-	-	291.79	258.62	-	-
PANSS Positive Symptoms	-	-	15.38	4.75	-	-
PANSS Negative Symptoms	-	-	14.38	5.09	-	-
PANSS General Psychopathology	-	-	29.66	7.63	-	-
PANSS Total Psychopathology	-	-	59.44	13.75	-	-

Table S1. Schizophrenia and Matched Healthy Comparison Subjects Sample Demographics. HCS, Healthy Comparison Subjects; SCZ; Patients diagnosed with Schizophrenia; PANSS, Positive and Negative Syndrome Scale; M, Mean; SD, Standard Deviation. Education level for the COBRE sample was determined based on the following scale: Grade 6 or less=1; Grade 7–11=2; high school graduate=3; attended college=4; graduated 2 years college=5; graduated 4 years college=6; attended graduate or professional school=7; Completed graduate or professional school=8. Olin education data were converted from 'years of education' to the COBRE education scale in order to permit combining of education demographic data. Parental education for the Olin set was the average of the mother and father's education. CPZ, Chlorpromazine equivalents were calculated according to latest validated approaches (1). SNR (signal-to-noise ratio) was determined by obtaining the mean signal and standard deviation for a given slice across the relevant BOLD run, while excluding all non-brain voxels across all frames (2). * denotes a significant T statistic for the between-group t-test.

Table S2 | Clinical and Demographic Characteristics - Bipolar Sample

Characteristic	HCS (N=56)		BD (N=73)		Significance	
	M	S.D.	M	S.D.	T Value / Chi-Square	P Value (two-tailed)
Age (in years)	31.25	10.35	32.00	11.27	0.39	0.70
Gender (% male)	38.71		27.03		1.84	0.07
Paternal education (in years)	12.98	3.87	14.83	3.59	2.79*	0.01
Maternal education (in years)	13.63	2.58	13.99	2.60	0.78	0.44
Participant's education (in years)	15.11	2.10	14.22	1.90	2.51*	0.01
Signal-to-noise (SNR)	215.45	58.98	216.80	52.03	0.89	0.14
% Frames Flagged	9.74	10.44	11.24	9.78	0.41	0.84

Table S2. Bipolar Disorder and Matched Healthy Comparison Subjects Sample Demographics. M, Mean; SD, Standard Deviation; age, education levels, and parental education are expressed in years. *denotes a significant T statistic for the between-group t-test. For complete clinical details and clinical measures used for the bipolar sample please see prior studies (3).

X	Y	Z	Hemisphere	Anatomical Landmark	Peak Z value	Mean Z value	Cluster size (#voxels)
Whole-Brain Covariance Connectivity SCZ>HCS							
18	41	34	Right	Superior Frontal Gyrus	4.84	3.03	325
-13	30	44	Left	Superior Frontal Gyrus	4.32	3.10	526
-21	-40	-20	Left	Cerebellum	4.40	2.88	286
-36	10	53	Left	Middle Frontal Gyrus BA 6	4.32	3.16	371
20	-5	58	Right	Middle Frontal Gyrus BA 6	4.30	2.97	494
14	17	54	Right	Superior Frontal Gyrus	4.29	2.95	433
32	9	37	Right	Sub-Gyral Frontal Lobe	4.13	2.80	447
-8	11	66	Midline	Superior Frontal Gyrus BA 6	4.09	2.87	334
-22	-06	55	Left	Sub-Gyral Frontal Lobe	4.13	2.92	405
31	35	19	Right	Sub-Gyral Frontal Lobe	4.02	2.93	430
-46	33	-10	Left	Inferior Frontal Gyrus	3.94	2.96	124
-39	15	29	Left	Middle Frontal Gyrus	3.91	2.90	326
13	-35	-13	Right	Cerebellum	3.98	2.76	220
-51	-56	40	Left	Inferior Parietal Lobule BA 40	3.93	2.66	302
-47	-16	-18	Left	Sub-Gyral Temporal Lobe	3.87	2.70	93
-11	-84	-40	Left	Cerebellum	3.67	2.78	176
56	17	18	Right	Inferior Frontal Gyrus	3.77	2.68	114
-30	45	14	Left	Superior Frontal Gyrus	3.65	2.81	240
53	-14	-26	Right	Fusiform Gyrus	3.65	2.68	80
-2	-20	-16	Midline	Midbrain	4.38	2.86	283
-11	61	14	Left	Superior Frontal Gyrus	3.61	2.74	222
-22	37	-18	Left	Middle Frontal Gyrus BA 11	3.75	2.73	66
33	-76	-45	Right	Cerebellum	3.55	2.70	48
-2	-12	12	Midline	Extra-Nuclear Cerebrum	3.55	2.61	162
46	28	-5	Right	Inferior Frontal Gyrus	3.44	2.72	152
-40	-68	-31	Left	Cerebellum	3.42	2.65	95
13	5	7	Right	Extra-Nuclear Cerebrum	3.42	2.75	168
27	-71	59	Right	Parietal Lobe	3.37	2.70	66
56	6	35	Right	Precentral Gyrus	3.45	2.67	159
-12	-22	-33	Left	Pons	3.37	2.75	63
-54	-60	-9	Left	Inferior Temporal Gyrus	3.33	2.74	105
-29	16	-9	Left	BA 13	3.33	2.63	83
53	-46	-8	Right	Middle Temporal Gyrus	3.26	2.62	72
-5	10	-8	Midline	Anterior Cingulate	3.21	2.63	75
29	9	-15	Right	Inferior Frontal Gyrus BA 47	3.18	2.67	111
8	-81	-29	Midline	Cerebellum	3.26	2.66	115
42	-49	49	Right	Inferior Parietal Lobule BA 40	3.21	2.60	193
33	-70	-23	Right	Cerebellum	3.12	2.55	62
-40	52	-6	Left	Middle Frontal Gyrus	3.02	2.55	52
12	60	28	Right	Superior Frontal Gyrus BA 9	4.51	2.90	206
12	-55	-37	Right	Cerebellar Tonsil	2.99	2.59	43
-10	-54	-48	Midline	Cerebellum	3.07	2.60	65
16	-23	-36	Right	Pons	3.59	2.79	59
27	-21	-19	Right	Parahippocampal Gyrus	3.42	2.62	57
-44	28	12	Left	Inferior Frontal Gyrus	3.12	2.56	74
2	34	23	Midline	Anterior Cingulate Cortex	4.52	3.00	101
-53	3	37	Left	Precentral Gyrus BA 6	4.26	2.85	107
23	-25	12	Right	Thalamus	2.70	2.48	34
-59	8	14	Left	Inferior Frontal Gyrus BA 44	3.16	2.62	40

Table S3. Region Coordinates and Statistics for Whole-brain Voxel-wise Covariance Connectivity Analyses. SCZ, schizophrenia patients; HCS, healthy comparison subjects. All statistics were calculated across all voxels for the identified significant clusters presented in the group difference (SCZ>HCS) Z map in **Figure 1H**.

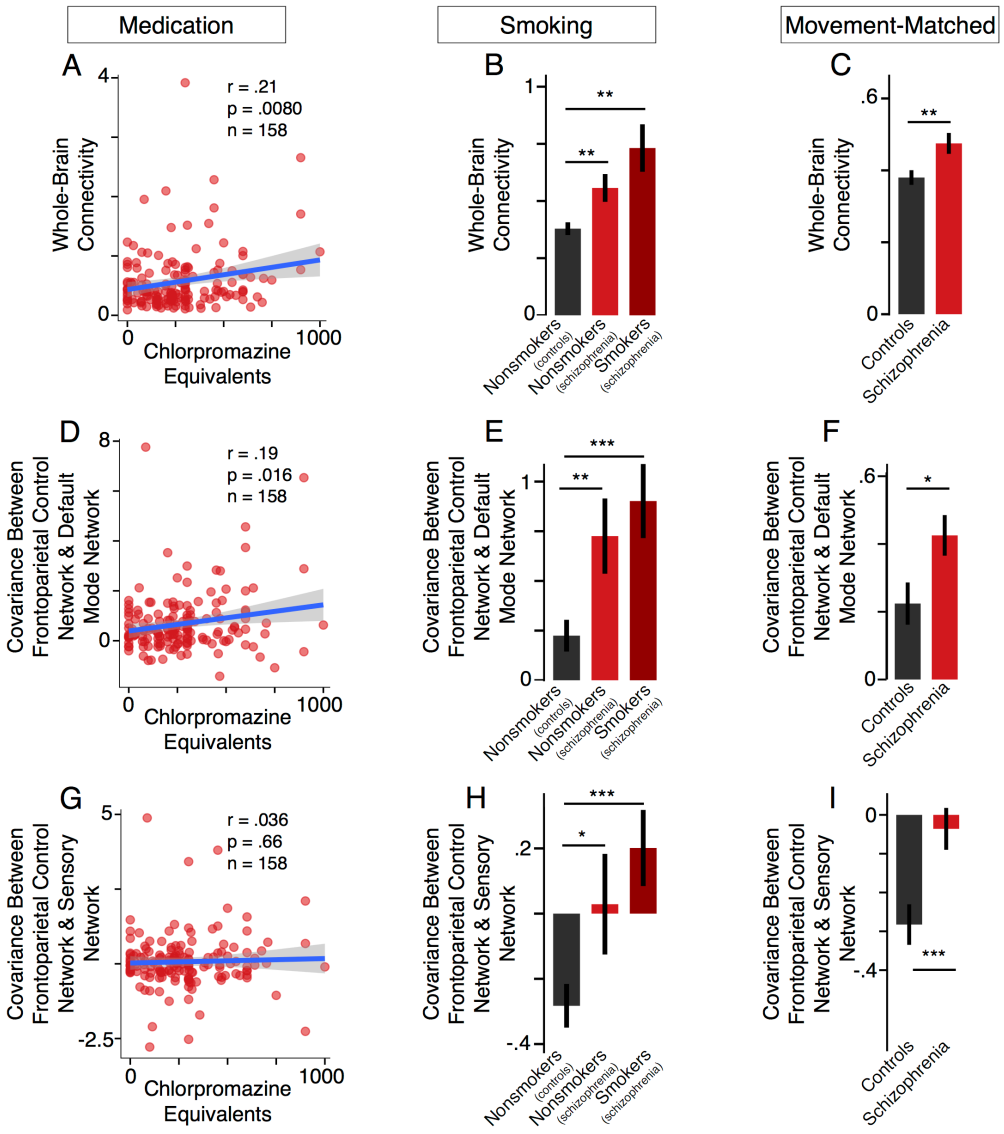

Figure S1. Examining Confounding Variables in Schizophrenia: Smoking, Medication and Movement. The magnitude of whole-brain connectivity (aka GBC, *a priori* analysis from **Fig.1F**) **(A)** and covariance between frontoparietal control network and default mode network (FPCN-DMN covariance) **(D)** (without global signal regression on preprocessed signal) showed a significant positive correlation with medication levels across subjects (all p-values <.05), calculated via chlorpromazine equivalent conversion (1). There was no significant correlation between covariance between frontoparietal control network and sensory network (FPCN-Sensory covariance) **(G)** and medication levels (p=.66). **(B**, **E**, **H)** The magnitude of whole-brain connectivity **(B)**, FPCN-DMN covariance **(E)**, and FPCN-Sensory covariance **(H)** (without global signal regression on preprocessed signal) is shown for healthy comparison subjects ("Controls") who were not smokers (N=90), patients with schizophrenia (SCZ) who were not smokers (N=59) and SCZ patients who were identified as smokers (N=46). All four measures were significantly increased for both smoker and nonsmoker patients relative to nonsmoker controls (p<.04, one-tailed test, for all measures). **(C**, **F**, **I)** Movement-matched subset. We identified a subset of participants (N=130 controls and N=130 patients) that were explicitly matched on the amount of frames flagged for movement (13.73% frames for patients and 13.64% frames for controls, p=0.53, one-tailed, n.s.). All three measures are significantly increased for patients relative to controls (all p-values <.02, one-tailed test) even when explicitly matched for number of flagged frames.

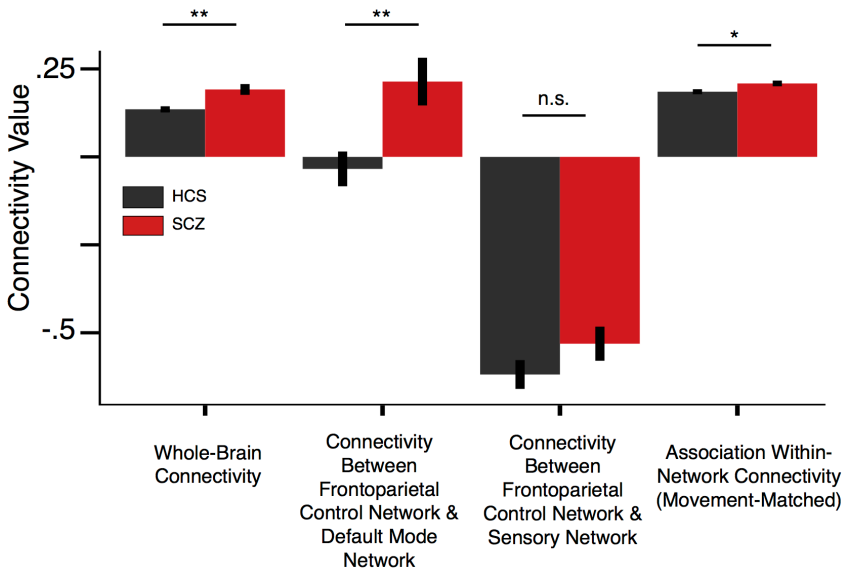

Figure S2. Findings After Global Signal Removal. Several presented connectivity measures from the main text were significantly different between groups when comparing patients with schizophrenia (SCZ) to healthy matched controls (HCS), without using global signal regression in data preprocessing. The bar plot shows the group-level results for these measures after global signal regression. Of note, all connectivity measures are covariance values and therefore without a standard unit. ** denotes p<.01. * denotes p<.05. n.s. = not significant. Whole-Brain Connectivity is the same as GBC (global brain connectivity) in the main text.

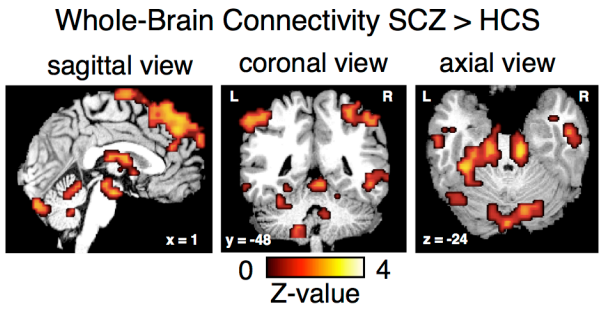

Figure S3. Volumetric Map of Whole-Brain Data-Driven Functional Connectivity Increases in Schizophrenia. Type I error corrected voxel-wise global brain connectivity (GBC) map computed using covariance as the measure of statistical dependence, revealing distributed increases in whole-brain connectivity for schizophrenia (SCZ) compared to healthy comparison subjects (HCS). The effect was particularly evident in association cortices (see **Figure 1-2**), thalamic, and cerebellar regions, which are highlighted here (see **Table S3**).

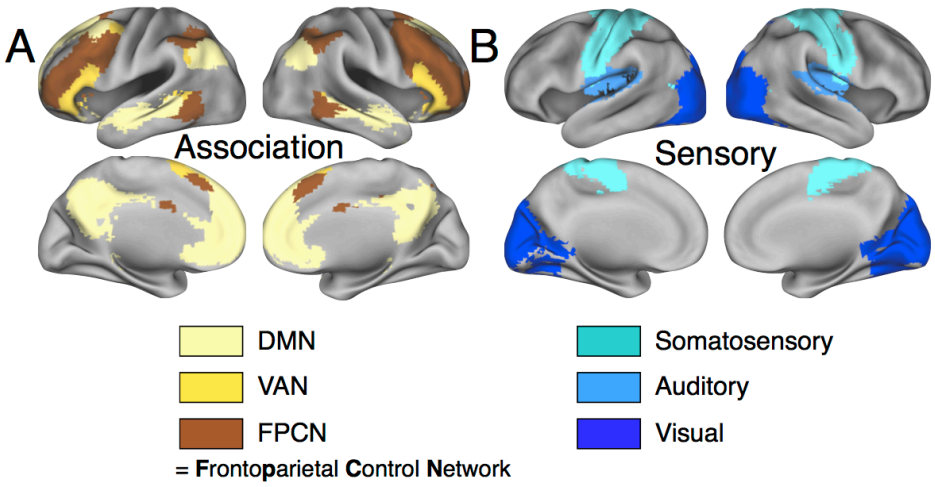

Figure S4. Association and Sensory Network Key. (A) Association networks: default-mode network (DMN) (light yellow), ventral attention network (VAN) (dark yellow), and the fronto-parietal control network (FPCN) (brown). **(B)** Sensory networks: somatosensory (cyan), auditory (blue), and visual (dark blue). These networks were obtained in volumetric format from Power and colleagues (4) then and mapped onto the surface using the Population-Average, Landmark- and Surface-based atlas (5).

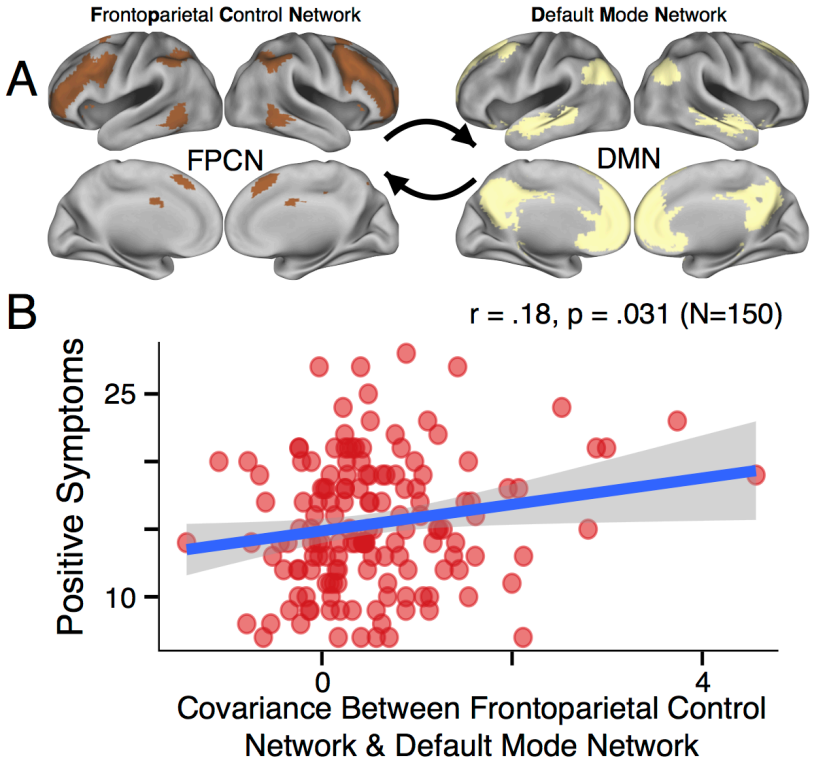

Figure S5. Symptom Correlations. (A) Between-network covariance was computed for DMN (left) and FPCN (right) in SCZ subjects. **(B)** Relationship between FPCN-DMN covariance magnitude and positive symptom severity [r=.18, p=.031, 2-tailed], quantified for patients with complete positive symptom data (n=150). FPCN=Frontoparietal Control Network, DMN=Default Mode Network.

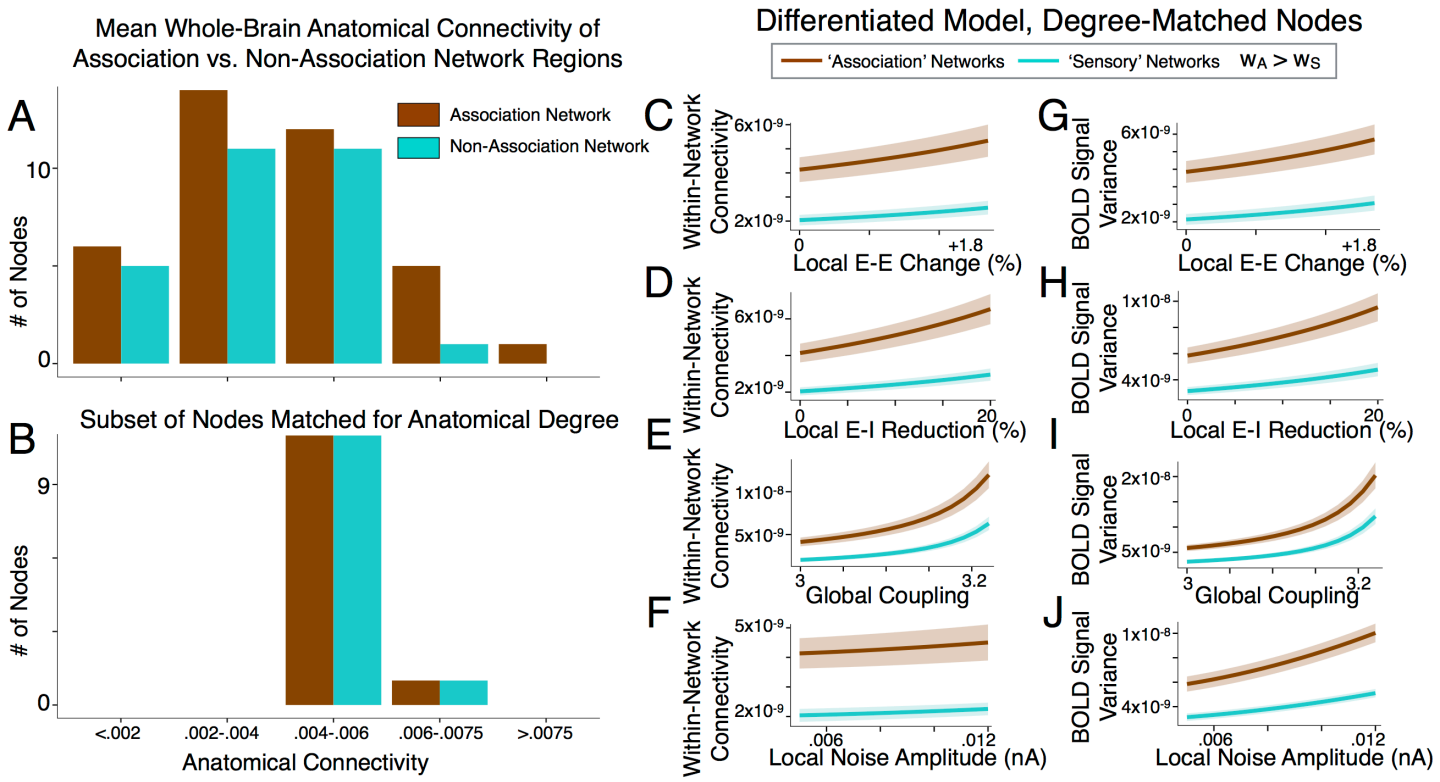

Figure S6. Mean Whole-Brain Anatomical Connectivity of Association vs. Non-Association Network Regions. (A) Histogram of anatomical connectivity for the 66 nodes of the model, which were coupled to each other using the human anatomical connectivity matrix obtained from the diffusion-weighted imaging study by Hagmann and colleagues (6, 7). Anatomical connectivity for each node was computed as the average of the mean column (structural outputs) and mean row (structural inputs) value for that node in the Hagmann matrix. Brown bars mark nodes belonging to association regions, teal bars to non-association regions (determined using the original parcellation employed by Hagmann and colleagues (7)). The distributions of anatomical degree for association vs. non-association nodes were not significantly different, assessed using a 2-sample Kolmogorov-Smirnov test [p=.93, test statistic=.13]. **(B)** To further highlight that preferential network-level model effects were predominantly driven by functional differences in local functional recurrence properties for association vs. non-association nodes (as opposed to the larger number of high-degree association nodes), we explicitly matched a subset of the model nodes on anatomical degree: 12 from the association network and 12 from the non-association network. Then, we computed within-network connectivity **(C-F)** and signal variance **(G-J)** of this matched subset of nodes as a function of our 4 key parameters manipulating E/I ratio, as done for the full set of nodes in **Figure 4** and **6**. Of note, we computed within-network connectivity for the 12 nodes of each network as the average connectivity with all other nodes from their respective networks and not only with other nodes in the chosen subset. Again, we observed that functional properties of nodes (local recurrence), rather than their anatomical degree, differentiate their sensitivity to E/I balance alterations.

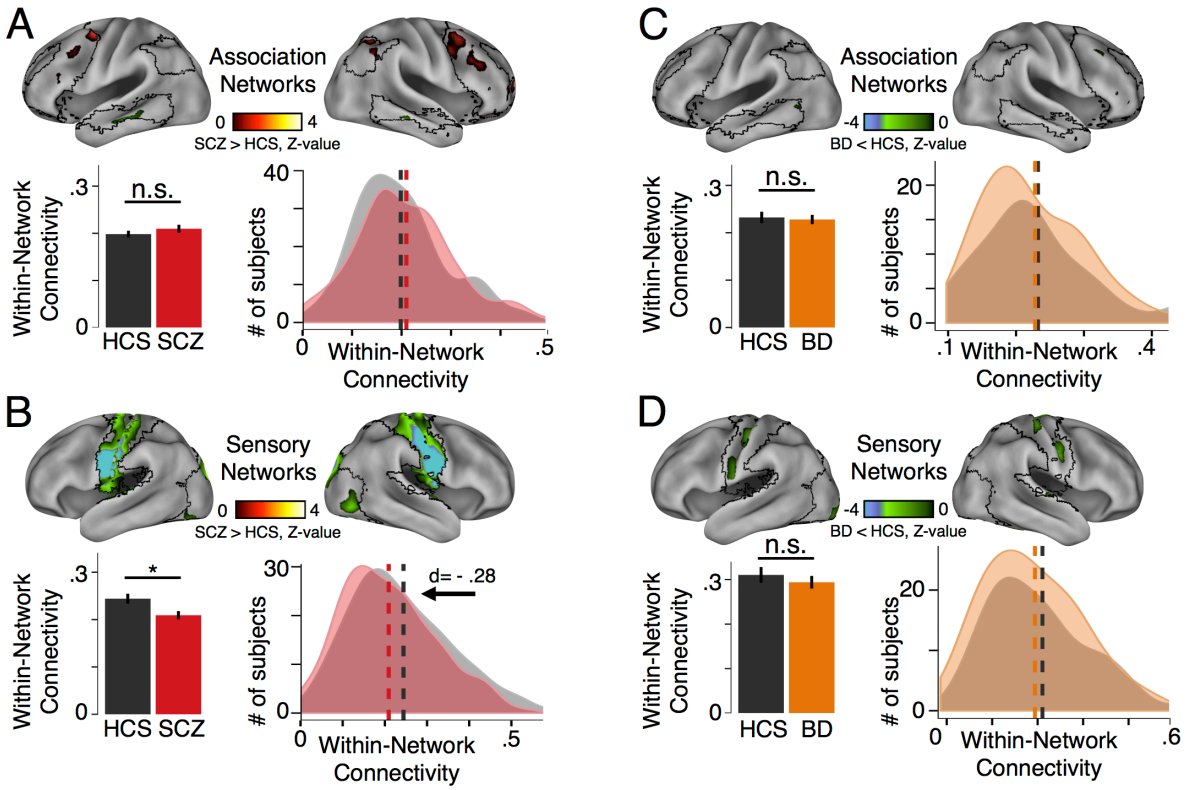

Figure S7. Preferential Network-Level Functional Connectivity Changes in Schizophrenia versus Bipolar Disorder Patients. (A) (Top) Between-group voxel-wise within-network connectivity Z-map showing association network regions (specifically DMN, FPCN, and VAN) (type I error corrected, see **Experimental Procedures**). (Bottom, left) Group-average for SCZ illustrates qualitatively elevated within-network connectivity for association networks compared to matched HCS, though effect is not significant for the full SCZ sample when including individuals with elevated motion parameters [p=.3]. (Bottom, right) Density histogram showing the sample distribution of average association within-network connectivity for each group (SCZ = red and HCS = black/gray). **(B)** Same analyses for the sensory networks, showing significant reduction of connectivity for sensory networks in SCZ compared to HCS [p=.011]. **(C-D)** Same analyses for BD sample. Error bars mark +/- 1 standard error of the mean. * denotes p<.05. Vertical dashed lines represent the group mean values.

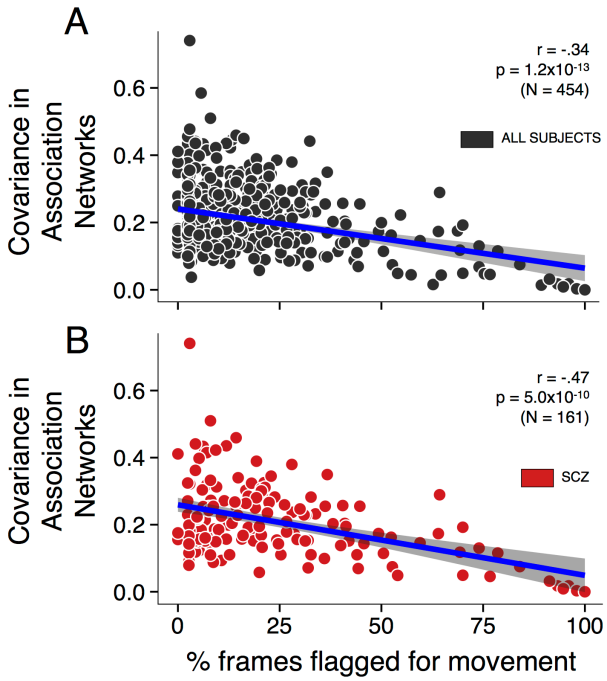

Figure S8. Relationship Between Movement Characteristics and Covariance in Association Networks. In the main text we explicitly reported movement-matched analyses where we selected subsets of SCZ and HCS participants that exhibited a similar amount of head motion (determined by % of frames that were flagged for movement). To further rule out the possibility that amount of head motion was related to the core reported effect, we quantified the relationship between the percentage of frames flagged for excessive movement (x-axis) and the magnitude of covariance within association networks (y-axis). **(A)** We show the relationship across all participants across all the samples (HCS, BD and SCZ, N=454), which revealed a significant negative relationship between the percentage of frames flagged for excessive movement and the magnitude of covariance within association networks (r(Pearson)=-.34, $p=1.2x10^{-13}$; r(Spearman)=-.16, $p=6x10^{-4}$, 2-tailed). **(B)** We repeated the same analysis only for the SCZ participants to ensure that the pattern remained unchanged (r(Pearson)=-.47, $p=5x10^{-10}$; r(Spearman)=-.29, $p=2x10^{-4}$, 2-tailed). Collectively, these analyses are strongly inconsistent with the possibility that higher levels of head motion were associated with higher association network covariance in the overall sample and in SCZ patients specifically.

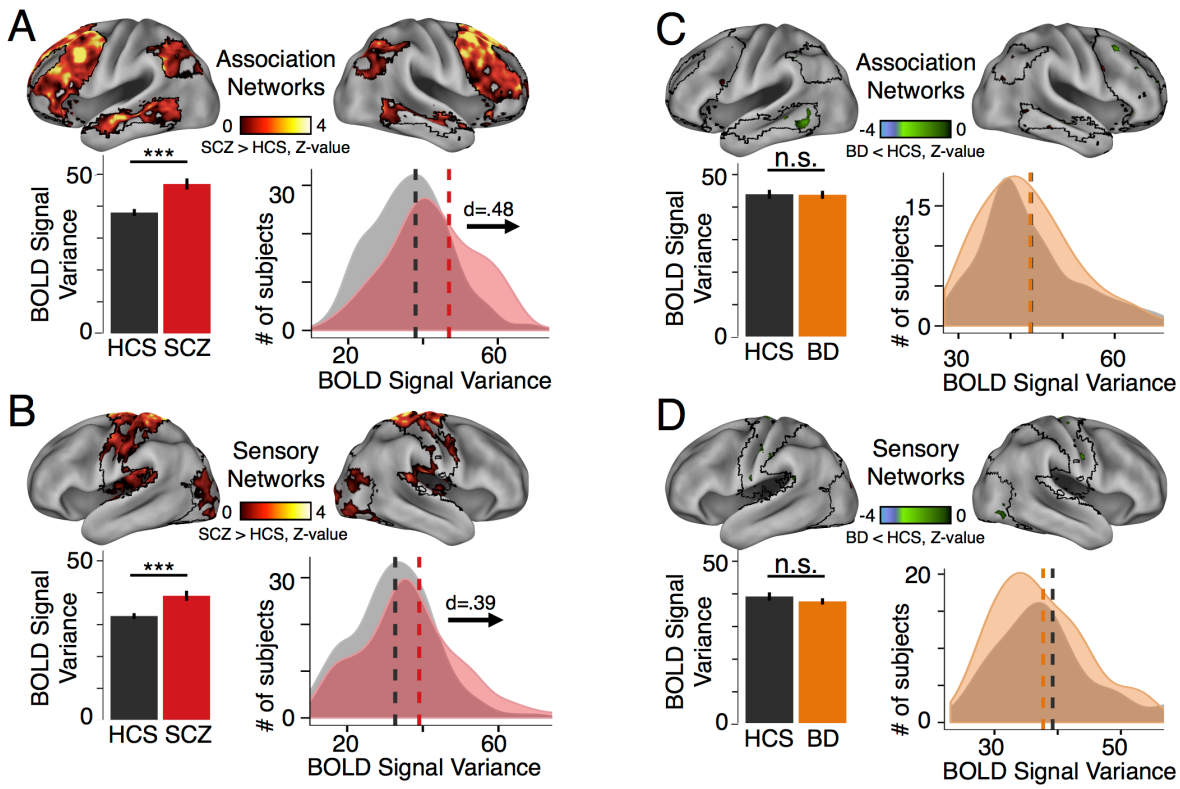

Figure S9. Preferential Network-Level Variance Changes in Schizophrenia versus Bipolar Disorder Patients. (A) (Top) Between-group voxel-wise BOLD signal variance Z-map restricted to association network regions (specifically DMN, FPCN, and VAN) (type I error corrected, see **Experimental Procedures**). (Bottom, left) Group-average for SCZ illustrates significantly elevated variance for association networks compared to matched HCS [$t(273)=4.32, p<2.2\times10^{-5}$]. (Bottom, right) Density histogram showing the sample variance distribution across association networks for each group (SCZ = red and HCS = black/gray). **(B)** Same analyses for the sensory networks. **(C-D)** Same analyses for BD sample. Error bars mark +/- 1 standard error of the mean. *** denotes p<.001. n.s. = not significant. d = Cohen's d effect size. Vertical dashed lines represent the group mean values.

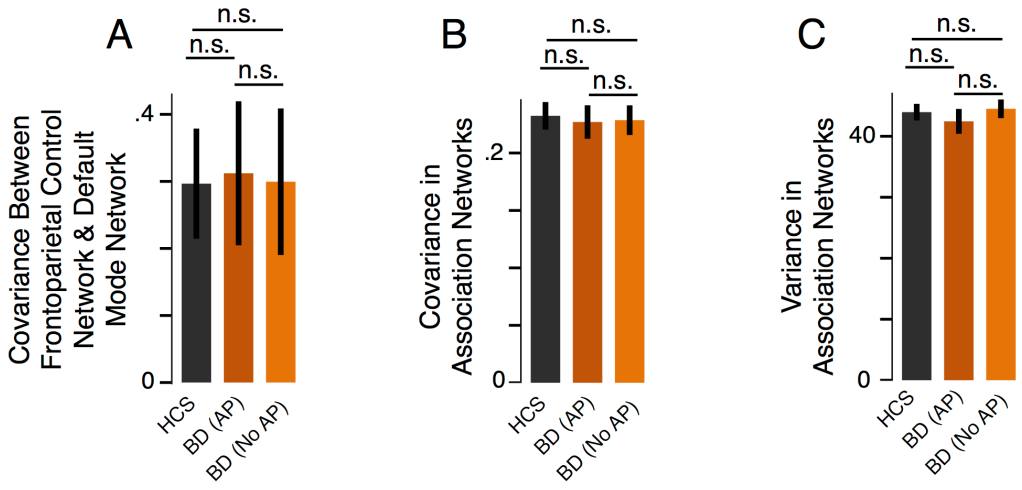

Figure S10. Examining Effects of Long-Term Antipsychotic Treatment on Covariance and Variance Effects in Bipolar Disorder. One concern that can be raised in the context of SCZ effects is the cumulative effects of antipsychotic treatment over extended periods of time, which may confound the observed effects. The cumulative medication impact is very difficult to quantify accurately, particularly the precise level and exact duration of compounding medication effects on brain function in SCZ. Here we attempted a proxy analysis that adds confidence that the core clinical SCZ effects are not confounded by medication. Specifically, we identified N=25 bipolar patients who were treated in conjunction with anti-psychotic (AP) medication during their illness course (BD AP). Next, we explicitly compared the FPCN-DMN between-network covariance (**A**), within-network covariance of association networks **(B)** and (**C**) association variance profiles between BD patients that received long-term antipsychotic treatment (BD AP) as well as those bipolar patients that were not treated by antipsychotics (BD No AP). We observed no significant differences across BD patients on and off antipsychotic medication, suggesting that the SCZ effect are less likely to be driven purely by long-term antipsychotic exposure. HCS = healthy comparison subjects from the BD sample. n.s. = not significant. FPCN=Frontoparietal Control Network, DMN=Default Mode Network.

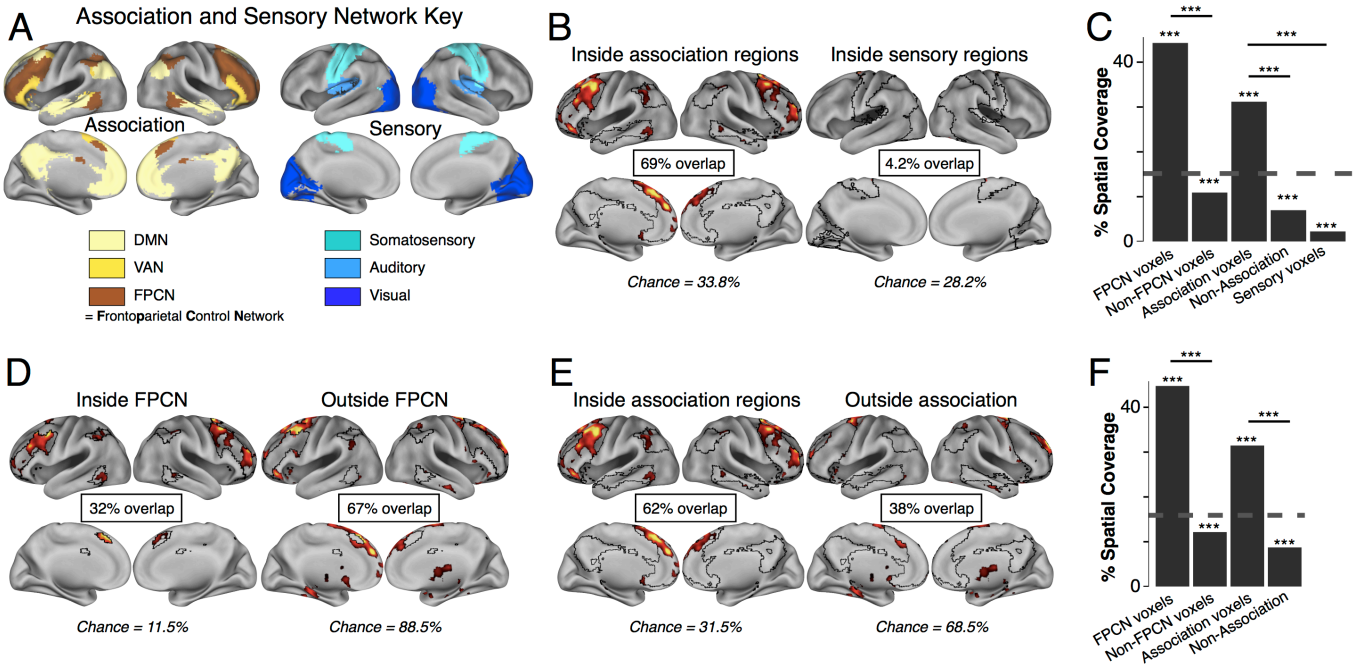

Figure S11. Quantifying Overlap Between Increased Whole-Brain Connectivity in SCZ & Independently Defined Association vs. Sensory Regions. (A) Using a priori defined, network-based parcellations, we defined areal boundaries for the association cortex (comprised of frontoparietal control network, default mode network, and ventral attention network), and the sensory cortex (comprised of somatosensory, auditory, and visual regions). **(B-C) Downsampled results. (B)** After downsampling images to 10mm-size voxels, to attenuate spatial correlations, 69% of areas showing elevated SCZ connectivity (**Figure 1H**) overlapped with the association regions (33.8% of total downsampled gray matter voxels belong to association regions). In contrast, 4.2% of areas showing elevated SCZ connectivity overlapped with sensory regions. Brain images are for visualization purposes only and have not been downsampled. **(C)** The significance above each bar represents the result from binomial tests computed for **(Figure 2B-C)** and for sensory networks **(B)**, comparing the expected percentage of significant voxels with the observed percentage of total significant voxels lying within each region (inside FPCN, outside FPCN, inside association, outside association, sensory networks). The percent spatial coverage plotted represents the total number of significant voxels in a region, divided by the total number of voxels for that region. The significance between bars marks difference between proportions, comparing spatial coverage within FPCN (or association cortex) with spatial coverage outside, or comparing spatial coverage in association regions vs. spatial coverage in sensory regions. The dashed line marks the spatial coverage of all gray matter voxels by significant voxels (see **Figure 1H** and **2**). **(D-F)** Binomial test results for quantifying overlap between increased whole-brain connectivity in SCZ and independently defined association regions *without downsampling* voxels. This is computed identically to what was done in **Figure 2B-D**, except voxels are not downsampled to 10-mm. **(D)** 32% of areas showing elevated SCZ connectivity (**Figure 1H**) overlapped with the FPCN (11.5% of total gray matter voxels belong to FPCN). In contrast, for the 'outside FPCN' region, defined as all cortical gray matter not belonging to FPCN, there was far less overlap with regions of elevated SCZ connectivity (67%) than expected by chance (88.5%). **(E)** We repeated analyses using all association networks (FPCN, DMN, and VAN), again showing preferential co-localization of elevated SCZ connectivity with association regions. Again, the 'outside association' region was defined as all cortical gray matter not belonging to the association region comprised of FPCN, DMN, ad VAN. **(F)** The significance above each bar represents the result from binomial tests computed for **(D-E)**, whereas the significance tests between bars represent differences between proportions of spatial overlap. The dashed line marks the spatial coverage of all gray matter voxels by significant voxels (see **Figure 1H**). *** denotes p<.001.

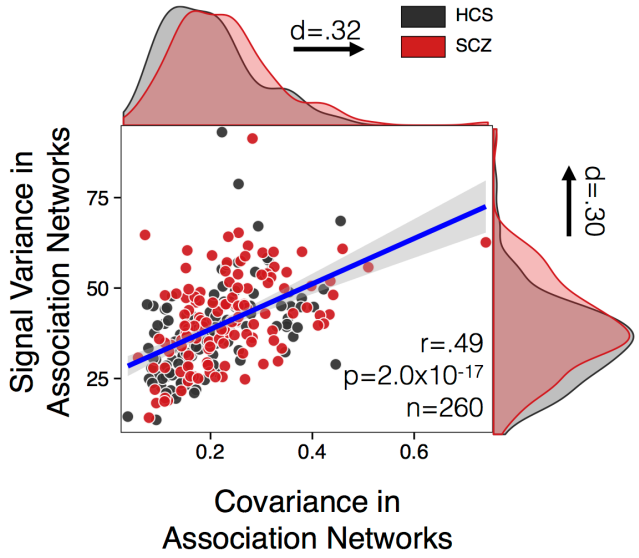

Figure S12. Within-Network Connectivity and Variance Are Correlated in Association Networks. Within-network connectivity **(Figure 5)** and BOLD signal variance **(Figure 7)** are plotted on the x and y axes, respectively, showing a strong positive relationship between these measures [r(Pearson)=.49, $p=2.0x10^{-17}$; r(Spearman)=.56, $p<2.2x10^{-16}$, N=260]. Group distributions of each measure are shown on the margins of the scatter plot, highlighting the mean significant effects for SCZ relative to HCS. d = Cohen's d effect size. The significant positive correlation remains even adjusting for the few extreme cases [r(Pearson)=.51, $p<2.2x10^{-16}$; r(Spearman)=.55, $p<2.2x10^{-16}$, N=257] and also holds in the SCZ sample alone [r(Pearson)=.45, $p<1x10^{-7}$; r(Spearman)=.47, $p<2x10^{-8}$, N=130].

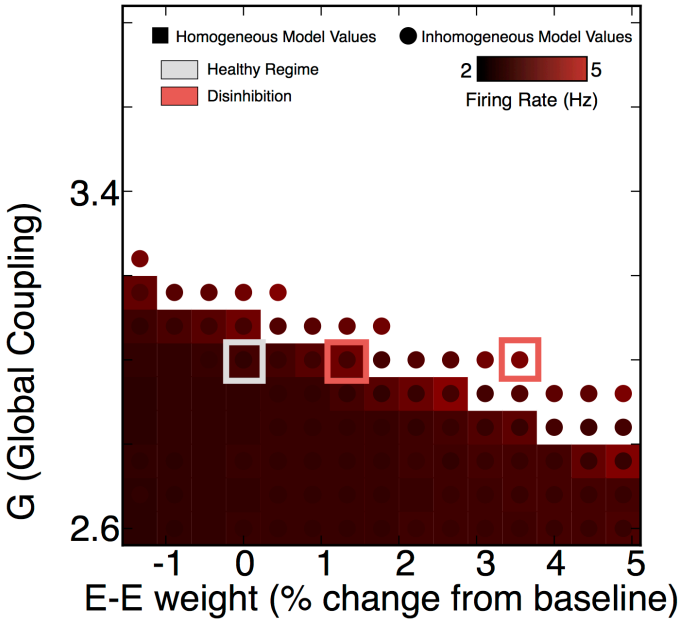

Figure S13. Parameterscape of Homogeneous and Inhomogeneous Model Stable Regimes. We explored the stable regimes of the homogeneous (circles) and inhomogeneous (squares) models by varying parameters G (global coupling) and E-E weight at values bordering the 'healthy' regime (G=3.0, E-E weight = 0% change from baseline). The colored circles and squares represent the maximum firing rates of the nodes in the model at various combinations of G and E-E weight. Firing rates > 5Hz were associated with regimes where the baseline state was unstable. White regions represent these unstable regimes. The light gray box marks the 'healthy' regime parameter values. The two red boxes represent examples of disinhibited states that the model would predict for schizophrenia. The red box to the far right shows an example of disinhibition for the inhomogeneous model, only—the homogeneous model is already destabilized at the point marked by the far right box. We speculate that the existence of sensory nodes in the inhomogeneous model creates additional stability in the sense that the sensory nodes are less easily drawn into disinhibition since they begin at a regime with only the low-firing-rate attractor state. The system as a whole is therefore able to tolerate more disinhibition before destabilizing. When the system does destabilize, it is drawn into the high-firing-rate attractor state by the subset of nodes belong to association regions.

SI EXPERIMENTAL PROCEDURES

Participant Inclusion Criteria and Characteristics. As noted in the main text, we studied two independent clinical samples: i) 161 chronic schizophrenia (SCZ) patients and 164 demographically matched healthy comparison subjects HCS (**Table S1**) recruited from the Olin Neuropsychiatry Research Center and from a publicly-distributed dataset provided by the Center for Biomedical Research Excellence (COBRE) (http://fcon_1000.projects.nitrc.org/indi/retro/cobre.html); ii) 73 patients diagnosed with bipolar disorder (BD) and 56 HCS, to test whether clinical effects generalize or are specific to SCZ (**Table S2**). Across samples, all subjects met identical neuroimaging exclusion criteria, underwent identical preprocessing and analyses (see analysis sections below).

The sample of SCZ participants recruited at the Olin Center (N=90) were identified through outpatient clinics and community mental health facilities in the Hartford (CT) area. Complete recruitment details for this sample are described in our prior work (8, 9). Briefly, patient inclusion criteria were as follows: i) SCZ diagnosis as determined by the Structured Clinical Interview (SCID) for the Diagnostic and Statistical Manual of Mental Disorders-IV (DSM-IV) (10), administered by experienced MA or PhD-level research clinicians; ii) no major medical or neurological conditions (e.g. epilepsy, migraine, head trauma with loss of consciousness); and iii) IQ>70 assessed by widely-accepted methods for estimating premorbid intelligence levels [either National Adult Reading Test (NART), Wide Range Achievement Test (WRAT) or Wechsler Test of Adult Reading (WTAR) depending on the study protocol] (11). As in our prior studies, these measures were normed and converted to IQ equivalents for each subject. If more than one premorbid achievement measure was available per subject, the scaled scores were averaged per standard practice (12). The 'IQ' measures are based on measures that assess premorbid academic achievement levels and do not capture more complex higher-order cognitive deficits (13). While this question is beyond the scope of our investigation, future studies should systematically examine if cognitive impairment relates to presently identified effects. In the present study we did not exclude patients with a lifetime co-morbid Axis I anxiety disorders and/or history of substance abuse in the SCZ sample to ensure an inclusive and representative sample of patients (14). However, all Olin SCZ sample participants were required to be fully remitted >6 months prior to the study. HCS (N=90) matched to SCZ patients were recruited through media advertisements and flyers posted in the Medical Center area. Inclusion criteria for HCS were: i) no current or lifetime Axis I psychiatric disorder as assessed by SCID-NP; ii) no history of medical or neurological conditions; and iii) no history of psychotic disorders in first-degree relatives (reported by detailed family history). The BD participants (N=73) and their respective matched HCS (N=56) were also recruited at the Olin Neuropsychiatry Research Center. The same general exclusion/inclusion criteria were applied, described previously in more detail (3, 15, 16).

As noted, the second SCZ sample was provided to the neuroimaging community by the Centers of Biomedical Research Excellence (COBRE) researchers. Critically, this large and independent SCZ sample has been extensively characterized, demographically matched and quality-assured across a number of prior reports (http://fcon_1000.projects.nitrc.org/indi/retro/cobre.html). SCZ patients recruited by the COBRE initiative were excluded if they had: i) history of neurological disorder, ii) history of mental retardation, ii) history of severe head trauma with more than 5 minutes loss of consciousness; iv) history of substance abuse or dependence within the last 12 months. Diagnostic decisions were reached using the SCID interview for the DSM-IV. Collectively, these criteria and demographics are highly comparable across the two SCZ samples.

To allow full inspection of clinical samples we provide complete demographics details in **Tables S1-2**. Across all samples we accomplished matching on a number of relevant demographic variables, ensuring comparable between-group demographic characteristics. The Olin sample groups were age and gender matched and did not significantly differ on any of the variables (see **Table S1**), apart from educational attainment and premorbid intellectual functioning (IQ) (see aforementioned comments). Educational achievement was lower for SCZ patients, and likely reflects the shortened educational achievement for patients due to illness onset (17). As these differences are impacted by the illness course, they were not considered as a covariate as they likely reflect illness trajectory. Notably, smoking status did not alter reported effects for the combined SCZ sample (see **Figure S1** for comprehensive confound analyses). 75/90 Olin SCZ patients were receiving antipsychotic treatment. SCZ patients for the COBRE sample were also receiving stable doses of antipsychotic medication with no medication changes for at least 1 month. All medication were converted to

chlorpromazine (CPZ) equivalents (1) and examined as continuous covariates in our analyses (see **Figure S1**).

Schizophrenia Symptoms. SCZ symptom severity, across both samples, was determined using the Positive and Negative Syndrome Scale (PANSS), a widely-used symptom instrument, which captures positive, negative and general psychopathology symptom dimensions (18) (**Table S1**). BD patients were in remission at the time of the scan (3), therefore no symptom analyses were attempted.

Neuroimaging Acquisition. Subjects were recruited at the Olin Neuropsychiatry Research Center and were scanned using a Siemens Allegra 3T scanner (3). Specifically, images sensitive to BOLD signal were acquired with axial slices parallel to the anterior-posterior commissure (AC-PC) using a T2*-weighted gradient-echo, echo-planar sequence (TR/TE=1500/27ms, flip angle=60°, field of view=24x24cm, acquisition matrix=64x64, voxel size=3.43x3.43x4mm) covering the whole brain. The acquisition lasted 5.25 minutes and produced 210 volumetric images per subject (29 slices/volume, inter-slice gap=1mm). Structural images were acquired using a T1-weighted, 3D magnetization-prepared rapid gradient-echo (MPRAGE) sequence (TR/TE/TI=2200/4.13/766ms, flip angle=13°, voxel size [isotropic]=.8mm, image size=240x320x208 voxels), with axial slices parallel to the AC-PC line. Subjects that comprised the COBRE sample underwent data collection at Center for Biomedical Research Excellence using a Siemens Tim-Trio 3T scanner. Full acquisition details for the COBRE SCZ sample and HCS is detailed previously (19-21). Briefly, BOLD signal was collected with 32 axial slices parallel to the AC-PC using a T2*- weighted gradient-echo, echo-planar sequence (TR/TE=2000/29ms, flip angle=75°, acquisition matrix=64x64, voxel size=3x3x4mm). The acquisition lasted 5 minutes and produced 150 volumetric images per subject. Structural images were acquired using a 6 minute T1-weighted, 3D MPRAGE sequence (TR/TE/TI=2530/[1.64, 3.5, 5.36, 7.22, 9.08]/900, flip angle=7°, voxel size [isotropic]=1mm, image size=256x256x176 voxels) with axial slices parallel to the AC-PC line.

Neuroimaging Preprocessing. Preprocessing followed our prior validated approaches that were applied to clinical populations (3, 16). Critically, we performed identical preprocessing procedures across all subjects collected across scanners, which were then registered to the same common standard space and interpolated to the same resolution. We performed the following basic preprocessing steps for all BOLD images, as done in our prior studies (3, 16): i) slice-time correction, ii) first 5 images removed from each run, iii) rigid body motion correction, iv) 12-parameter affine transform of the structural image to the Talairach coordinate system, and v) co-registration of volumes to the structural image with 3x3x3mm re-sampling, ensuring all BOLD images across both scanners were interpolated to the same resolution. In addition, all BOLD images had to pass stringent quality assurance criteria to ensure that all functional data were of comparable and high quality: i) signal-to-noise ratios (SNR)>100, computed by obtaining the mean signal and standard deviation (sd) for a given slice across the BOLD run, while excluding all non-brain voxels across all frames (3) (see **Tables S1-2**); ii) movement scrubbing as recommended by Power et al. (22, 23). “Movement scrubbing” refers to the practice of removing BOLD volumes that have been flagged for high motion, in order to minimize movement artifacts, and is a widely used fMRI preprocessing technique. Specifically, to further remove head motion artifacts, as accomplished previously (24), all image frames with possible movement-induced artifactual fluctuations in intensity were identified via two criteria: First, frames in which sum of the displacement across all 6 rigid body movement correction parameters exceeded .5mm (assuming 50mm cortical sphere radius) were identified; Second, root mean square (RMS) of differences in intensity between the current and preceding frame was computed across all voxels divided by mean intensity and normalized to time series median. Frames in which normalized RMS exceeded the value of 3 were identified. The frames flagged by either criterion were marked for exclusion (logical or), as well as the one preceding and two frames following the flagged frame. Movement scrubbing was performed for all reported analyses across all subjects.

Functional connectivity preprocessing followed best practices in the functional connectivity literature and was consistent with our prior studies (25). Specifically, to remove spurious signal in resting-state data we completed additional preprocessing steps, as is standard practice (26): all BOLD time-series underwent high pass temporal filtering (>.009 Hz), removal of nuisance signal extracted from anatomically-defined ventricles, white matter, and the remaining brain voxels (i.e. global signal) (all identified via individual-specific FreeSurfer

segmentations (27)), as well as 6 rigid-body motion correction parameters, and their first derivatives using previously validated in-house Matlab tools (28).

Whole-Brain Data-Driven Connectivity Analysis. To test the initial model-generated predictions of elevated connectivity we used a fully data-driven approach across all gray matter voxels. The data-driven *global brain connectivity* (GBC) approach (16, 29) was applied using in-house Matlab tools. GBC, originally reported using correlation computations, provides a more sensitive connectivity measure by computing covariance (GBCcov) strength of each voxel with all other voxels being considered. As described previously (3, 16, 29), GBC is designed to estimate the connectivity between each individual voxel and every other voxel in the brain or a restricted search space (e.g. a given network, which we detail below). Before GBC analysis, BOLD signal within the subject-specific cortical mask was spatially smoothed with a 6mm full-width-at-half-maximum (FWHM) Gaussian kernel and dilated by two voxels (6mm) to account for individual differences in anatomy.

Briefly, "spatial smoothing" means that voxels within each volumetric image are averaged with their spatially adjacent neighboring voxels. A common method used to implement spatial smoothing in fMRI is to convolve the fMRI signal with a Gaussian function of a specific width. "Dilated by two voxels" refers to the mask used (e.g. the individual's whole brain mask), which was radially dilated by two voxels. Smoothing and dilation are performed to minimize individual differences in anatomy and improve signal-to-noise owing to imperfect volumetric registration. This is a technique we have used in our prior studies when applying the GBC metric (3, 16, 29, 30).

Finally, for each gray matter voxel, we computed covariance with every other gray matter voxel, and then computed their mean for a given subject. This calculation yielded a whole-brain GBC map for each subject where each voxel value represents the mean connectivity of that voxel with other gray matter voxels in the brain.

Besides voxel-wise GBC, we also computed the average whole-brain connectivity alteration in SCZ relative to HCS (**Figure 1F**). As noted, GBC is a fully data-driven procedure, producing a connectivity value for each voxel with every other voxel in the brain. Initially, we sought to test model-generated predictions across all gray-matter voxels. To quantify 'average' whole-brain GBC for each subject we data-reduced our GBC analysis using a well-validated large-scale network parcellation. For this *a priori* analysis, we selected a well-established and validated large-scale network parcellation established by Power and colleagues (4), which was comprised of 89 ROIs in total, derived from 25 distinct networks. To render the average whole-brain GBC analysis more computationally tractable we conducted GBC analyses across 89 ROIs for **Figure 1F**-**G**. This effectively yielded a single whole-brain GBC value for each subject. To compute between-group contrasts we used individual subject voxel-wise GBC covariance maps (**Figure 1H**, see **2nd-Level Group Comparisons** below).

Network-Specific Analyses: Network Selection and Signal Extraction. Across a number of analyses we focused on sets of specific large-scale networks. We used *a priori* regions that were part of a well-validated large-scale whole-brain parcellation (4) (see **Figure S4** for an overview of all large-scale networks used). These networks included: default-mode network (DMN), ventral attention network (VAN), fronto-parietal control network (FPCN), somatosensory, auditory, and visual network. In turn, we combined the somatosensory, auditory, and visual networks into a large 'sensory network' signal (**Figure S4,** blue areas). We combined the DMN, VAN and FPCN into the 'association network signal (**Figure S4,** yellow-brown areas). The logic here is that main model predictions regarding the cortical hierarchy were generated with respect to two pools of nodes: 'association' and 'sensory', with higher and lower levels of local recurrence respectively (see **Computational Modeling** below).

Quantifying Network Overlap. Our initial fully data-driven analyses generated a result that qualitatively co-localized to association cortex (with the exception of cerebellar and thalamic signals that were outside of the scope of our current model architecture). To formally quantify this co-localization, we first downsampled our whole-brain t-maps to 10mm-size voxels in order to remove spatial correlations. Then we computed the percent of overlap between the between-group contrast map reported in **Figure 1** and the FPCN and association networks more broadly, as well as the sensory networks (visual, somatosensory, and auditory

combined) as a control analysis. In turn we used the binomial probability test to statistically test the observed overlap given the level of overlap expected by chance (31). We used the test for difference between proportions to test whether the spatial coverage of FPCN was significantly different from the spatial coverage of non-FPCN regions, and similarly compared the association networks region to the remaining gray matter. As an additional control analysis, we compared association networks to sensory networks in **Figure S11**. To clarify, both "observed overlap" and "spatial coverage" consider the quantity of voxels from the between-group contrast map that fall within the region of interest. However, "observed overlap" divides this quantity by the total number of contrast map voxels, and "spatial coverage" divides this quantity by the total number of gray matter voxels within the region of interest.

Network-Specific Analyses: Within- and Between-Network Analyses. As reported in the main text, we computed two distinct network-level analyses: i) within a given large-scale network, ii) between pairs of large-scale networks.

Within-network Connectivity. To compute within-network connectivity, we used the identical data-driven GBC procedure as described above, only restricted to a given network (e.g. DMN). In this case we calculated the 'restricted' GBC (or rGBC) for each gray matter voxel within a given network with all other gray matter voxels within that network. This effectively yielded a 'within-network' rGBC that allowed us to quantify the level of connectivity alteration for a given cortical network. This level of analysis (i.e. network-level) was explicitly designed to test model-generated predictions following the expansion of the architecture to include a functional cortical hierarchy (see **Figure 4** and details on computational modeling below). Of note, to compute within-network connectivity of the 'sensory' network, we computed results for each sensory network separately, and then averaged the three final sensory networks. We also examined the somatosensory network specifically as a control analysis. We found very similar results to those obtained using the combined sensory networks. Similarly, within-network connectivity of the 'association' network was the average of the rGBC computed separately for each of the three association networks.

Between-network Connectivity. To conduct between-network connectivity analyses (see **Figure 3**), we computed the covariance between pairs of signals representing the spatially averaged time series for pairs of large-scale networks: i) FPCN and DMN; ii) FPCN and sensory network regions (see network selection above); iii) DMN and sensory network regions. The covariance value obtained was used as the measure of between-network connectivity. Note that when computing between-network connectivity for FPCN-sensory or DMN-sensory covariance, we found results were qualitatively similar to the covariance values for FPCN-somatosensory and DMN-somatosensory between-network connectivity. FPCN-somatosensory covariance was significantly increased in SCZ compared to HCS [$t(262)=3.2$, $p=.0016$]. DMN-somatosensory covariance did not significantly differ between SCZ and HCS [$t(281)=0.5$, $p=.6$].

Choice of Functional Connectivity Measures. Across all reported analyses we used covariance as the measure of statistical dependence to measure functional connectivity, as opposed to Pearson's correlation coefficients (i.e. normalized covariance). As noted in the main text, the use of correlation as a metric for inferring functional connectivity between two regions may be problematic in some situations if there are differences in variance across groups. Mathematically, the correlation between X and Y is effectively normalized covariance, defined as the covariance between X and Y, divided by the standard deviation of X and the standard deviation of Y. As described in the main text, the magnitude of a computed correlation between X and Y can be spuriously reduced by increasing the baseline noise amplitude of one or both signals, without any real change in the absolute amount of shared variance (covariance) between the signals – a problem recently highlighted in SCZ (25, 32). Therefore, given the recently established alterations of BOLD signal variance in SCZ, we explicitly selected a functional connectivity metric (i.e. covariance) that is not sensitive to signal variance changes. In this way, we could avoid confounding group-level differences in covariance with group-level differences in measurement noise or endogenous variance unique to each region.

2nd-Level Group Comparisons. On several measures, HCS and patient groups displayed distributions of unequal variance, assessed using Levene's test. Therefore, all reported t-test values (except those for the Demographics in **Tables S1-2**) were computed without assuming equal variance. All 2nd level group analyses

were computed on covariance or variance maps. Collectively, we conducted several separate group-level analyses: i) We computed the GBC analyses at the whole-brain level (i.e. all gray matter voxels), in order to test initial model-generated predictions (see **Figure 1**); ii) We computed differences between patients and controls for both covariance and variance within specific *a priori* large-scale networks (see **Figure S4** for network selection). Each of the network-level analyses were appropriately corrected for type I error within the network mask. Type I error correction for a given analysis was ascertained via peak and cluster extent based on permutation testing (33). Results were visualized using Caret 5.5 software (http://brainvis.wustl.edu/wiki/index.php/Caret) and NeuroLens software (http://www.neurolens.org). Unless otherwise noted, fMRI results are presented without global signal removal (GSR), a preprocessing step that may potentially remove clinically meaningful information (25, 34). As noted above, when used as a control analysis, GSR was performed via standard procedures (35) using individual-specific whole-brain masks (excluding ventricle and white-matter voxels). We verified that our core effects remained present after GSR (see **Figure S2**).

Computational Modeling. We employed a validated computational model of resting-state brain activity (6, 25, 36), extending a local dynamic mean field model (37) to incorporate biologically plausible mechanisms for BOLD signal fluctuations. Our model is composed of 66 nodes, each node composed of separate excitatory (E) and inhibitory (I) pools, representing local population activity of excitatory and inhibitory neurons. The E pools are coupled through a large-scale, inter-areal anatomical connectivity matrix, which was derived from diffusion tractography in humans as reported in Hagmann et al. (7) and used by Deco et al. (6, 36). The I pools provide local recurrent inhibition, supporting network stability. In particular, the inhibition strengths of the I pools vary by node to maintain a uniform baseline firing rate in E cells (~3Hz). The inhibition strengths correspond to E-I coupling, related to "E-I weight" in the main text. Specifically, the inhibition strengths are scalar multipliers for E-I weight. E-I weight is uniform across nodes, but inhibition strengths vary across nodes as determined by a machine-learning algorithm used to calibrate inhibition strengths at each node such that all E pools (in all nodes) could maintain the ~3 Hz firing rate at baseline. In all presented model manipulations, parameter values starting at the origin represent the 'healthy' regime, wherein E and I are balanced and the firing rate in all nodes is ~ 3 Hz. Parameter values are then perturbed toward elevated E/I up to the point before the model destabilizes to a regime of unrealistically elevated firing rates of simulated neurons.

Diffusion-Weighted Imaging (DWI) Structural Matrix. As noted, we coupled the model through a large-scale, inter-areal anatomical connectivity matrix, which was derived from diffusion tractography in humans as reported in Hagmann et al (7). The biophysical model is intended to generate activity based only on assumed direct connections between excitatory pools, and furthermore assumes relatively sparse connectivity amongst nodes, as is typically found in neuroanatomical studies using tracers (38). Critically, this method of constraining the neurodynamical model using structural architecture has previously been developed and validated by Deco and colleagues (6, 36) and in turn applied for generating clinical inference (25). A key advantage of using the DWI structural matrix in the model is that this precise constraint relates to a central finding of our study. Specifically, an important extension of the original model is the implementation of a functional hierarchy (called the "differentiated" model). Here we show that this *functional* hierarchy—rather than the *anatomical* hierarchy imposed from the DWI data—produces increased vulnerability of association nodes to disinhibition. This effect stood in contrast to the *functionally* undifferentiated model, which was also constrained by the same DWI data (i.e. it retained anatomical hierarchy properties). Put differently, both versions of the model (functionally differentiated and undifferentiated) use the identical structural connectivity DWI matrix. If we had instead used a functional parcellation and functional connectivity strengths to constrain node-to-node connections, we would not be able to contrast anatomical hierarchy effects with functional hierarchy effects.

Undifferentiated Model. Initially we started from a model architecture where all nodes were modeled with identical local recurrent properties – i.e. the model was undifferentiated with respect to local recurrent patterns across nodes. Generally, our model closely follows the feedback inhibition control (FIC) model reported by Deco et al. (36), except that we also include a globally-shared noise component corresponding to empirically observed global signal (GS) in resting-state fMRI studies (25). BOLD signals were simulated via the Balloon-Windkessel model, as done previously (6, 25, 36). We parametrically varied strengths of recurrent local self-excitation (E-E weight) within E pools of nodes, global coupling (G) between E pools of nodes,

amplitude of random noise (σ) within the E pools, and strength of recurrent inhibition provided by the I pools (E-I weight). Specifically, E-I weight refers to the local coupling of E pools to their corresponding I pools, and the degree to which activity in the E pools stimulates feedback inhibition from the I pools. Default starting values were set to E-E weight=.12 nA, G=3, σ=.005 nA, and E-I weight=1. Here we also set the noise amplitude of I pools to .002 nA. All other parameter values were set to those of Deco and colleagues (36). Of note, the model implemented by Deco and colleagues contained a net E-E weight term that was the product of two other terms, J_N (E-E weight) and w (a scalar multiplier that we set to be higher in association than in sensory nodes).

Next, to realistically capture the percentage of BOLD signal variance represented by the GS variance (25), we introduced a common input to all nodes, mimicking baseline low-level correlations seen empirically in gray matter. Specifically, a shared (global) noise term of amplitude .005 nA was added to the signal of all nodes, in addition to the unshared (local) noise term of .005 nA amplitude. This is a similar proportion of shared and unshared noise to what we reported previously (25). For our simulations of elevated E/I ratio, we first calibrated the model within the 'healthy' regime of parameter values, allowing for a machine-learning algorithm to iteratively choose appropriate local inhibition weights for the 66 nodes so that the whole network would achieve a stable average firing rate of ~ 3 Hz (see Deco, 2014). Then, we parametrically increased E/I ratio in four different ways: by increasing the values of E-E weight, G, σ, or the percent reduction of E-I weight.

Differentiated Model. In turn, we expanded our model architecture where subsets of nodes were modeled with distinct local recurrent properties – i.e. the model was differentiated with respect to local recurrent patterns across nodes, effectively generating higher-order (association-like) and lower-order (sensory-like) recurrence patterns. We first separated model nodes into pools of 'association' and 'sensory' nodes based on their cortical location defined from the original implementation of the anatomical connectivity matrix developed by Hagmann and colleagues (7). Next, for the differentiated form of the model, we set the E-E weight for nodes belonging to association regions (as identified via the anatomical connectivity matrix) to 3x the value relative to the remaining non-association nodes, which were set to a default E-E weight of .045.

Then, we again used the same machine-learning algorithm as applied above to obtain the appropriate inhibition weights for I pools in the differentiated model, so as to maintain the uniform baseline E-cell firing rate (~3 Hz). Then, as before, we parametrically changed the four parameters to perturb the differentiated model away from its baseline regime. The default value of E-E weights was .045 nA in non-association nodes and .135 nA (i.e., 3*.045 nA) in association nodes. Of note, we set association nodes' E-E weight to 3x that of the non-association nodes because of previously reported empirical observations (39) in primate neurophysiology demonstrating that the timescales of baseline neuronal activity for higher-order association cortical regions (~300 ms) are roughly 3x the value of lower-order sensory regions (~100 ms) (39).

Machine-Learning Algorithm. This algorithm was the same in implementation regardless of whether the model was functionally differentiated or not. We first set all the local inhibition strengths in the model to 1 at each node, as a starting point. Then we simulated neural activity for a period of 10 seconds, and computed the average firing rate of the local excitatory pool of each brain area, i.e. r_i for the firing rate at region *i*. If $r_i > 3.098$ Hz, we increased the corresponding local feedback inhibition Ji = Ji $+10^{-16}$; if $r_i < 3.082$ Hz, we reduced Ji = Ji - 10^{-16}. We repeated this procedure until the constraint on the firing rate of the local excitatory pool was fulfilled in all 66 nodes of the model.

Quantitative Model Comparison. Briefly, for **Figure 8**, we compared the undifferentiated and functionally differentiated models on their respective ability to reproduce empirical effects. To formalize our assessment of these competing models, we quantitatively compared them by projecting their predictions into a 4-dimensional space representing four key dependent measures: predicted change for association region within-network connectivity, for sensory region within-network connectivity, for association region BOLD variance, and for sensory region BOLD variance.

Within this 4-dimensional space, each model simulation can be represented as a vector pointing out of the origin. The origin in this case would be defined as the connectivity and variance values produced by the model when using 'healthy' regime parameter values (E-E weight = default values described above for Differentiated and Undifferentiated Models, G=3, E-I weight = 1, σ=.005 nA). All vectors arising from individual model simulations at disinhibited values of E-E weight, G, E-I weight, or σ, would therefore be computed in terms of *change* relative to the 'healthy' regime represented at the origin. Importantly, we found that individual

model simulations fell closely along the same line out of the origin, regardless of the severity of disinhibition (amount of increase in excitation/inhibition). Therefore, we represented each model (differentiated vs. undifferentiated; aka inhomogeneous vs. homogeneous) as a single vector arising from E-E weight increase, E-I weight reduction, G increase, or sigma increase. The vectors were slightly different depending on the parameter being manipulated, so we assessment the homogeneous vs. inhomogeneous models separately for each of the four parameter manipulations.

Using the two vectors obtained for each parameter manipulation, we computed the cosine similarity between model predictions (vectors) and empirically observed differences ('changes') in SCZ compared to HCS (**Figure 8B-E**). Specifically, the empirical data was represented in our 4-dimensional space using HCS group mean values as the "origin" with respect to the direction of 'change' in dependent measures observed in the SCZ group. Conceptually, this followed the model's simulations of E/I increases causing changes in the four dependent measures *relative* to the 'healthy' regime values for those four dependent measures.

Finally, we randomly permuted the network assignments (association vs. non-association) for all model nodes for 1,000 iterations in order to establish the cosine similarity expected by chance between the models and the empirical data, as well as the difference in cosine similarity expected by chance for the differentiated (inhomogeneous) model minus the undifferentiated (homogeneous) model (**Figure 8F-I**). Specifically, we used the identical BOLD signals arising from model simulations described above, and shuffled network labels (association vs. non-association) for model nodes. After shuffling, we re-computed the within-network connectivity and average BOLD signal variance for the new 'association' network and new 'sensory' networks and projected the shuffled models' predictions of change in each of these measures (relative to 'healthy' baseline) into the 4-dimensional prediction space. Using model vectors produced by this method, we computed cosine similarity between model vectors and the empirical data, as done before. Next, we found the difference between shuffled models with respect to their cosine similarity to empirical data, as done above for unshuffled models. As expected, the difference between models hovered near zero when node assignments were randomly permuted. The 1,000 permutations further allowed us to establish a 95% confidence interval for the expected difference in model performance for the differentiated vs. undifferentiated models, with respect to their cosine similarity to empirical data. Establishing the confidence interval allowed us to statistically confirm that the (un-permuted) differentiated model outperforms the undifferentiated model far beyond what would be expected by chance.

Matching Analyses at the Network Level Between Empirical and Model-generated Effects. As mentioned in the main text, for the computational model of resting-state cortical activity, we used the human anatomical connectivity matrix obtained from the diffusion-weighted imaging study by Hagmann et al (6, 7). This was a 66x66 anatomical connectivity matrix, with each of the 66 nodes labeled based on the anatomical location corresponding to the node. Therefore, we were able to classify nodes as 'association region' nodes or 'non-association region' on basis of anatomical labeling and connectivity included in the Hagmann matrix. Since the matrix was anatomically based, and not defined by functional connectivity, a one-to-one mapping of anatomical nodes to functional networks was not always feasible. However, we qualitatively found good correspondence of anatomical nodes to three different association networks: DMN, FPCN, and VAN, as well as good correspondence of anatomical nodes to three sensory networks: visual, auditory, and somatosensory. Therefore, we used the nodes falling within the anatomical boundaries of DMN, FPCN, VAN, and the three sensory networks as ROIs from which to extract connectivity measures at the corresponding functional network level. The ROIs representing DMN, FPCN, VAN, and the three sensory networks in the empirical data were obtained using a functional parcellation (not an anatomical parcellation), as described in **Network Signal Extraction** above.

SI DISCUSSION

Hyper-Connectivity Versus Hypo-Connectivity in Chronic Schizophrenia: Importance of Choosing Connectivity Metrics. Chronic SCZ has long been associated with altered functional connectivity, supported by emerging neuroimaging studies (9, 16, 25, 40-45). Many studies implicate PFC hypo-connectivity in chronic SCZ patients, including reduced within-region connectivity and reduced inter-connectivity between the PFC and the thalamus (9, 16, 45). At first, these effects seem at odds with presented elevated widespread connectivity (**Figure 1**). However, it is critical to note that the vast majority of prior studies (including our group) quantified functional connectivity using correlations as the measure of statistical dependence. The use of correlations as a method in this case may be inherently problematic (46), especially if there are regional differences in signal variance between groups (47). For instance, the magnitude of a computed correlation value between two signals can be spuriously reduced by increasing the baseline noise amplitude of one or both signals, without any real change in the absolute amount of shared variance (covariance) between the signals – a problem recently demonstrated in SCZ (25, 32). If functional connectivity is conceptualized to reflect the extent of 'shared signal' between regions, using correlation could result in artificially reduced connectivity measured between regions solely as an artifact of an increase in unshared noise in a setting of unchanged covariance. Indeed, given recent observations of elevated signal variance in SCZ (**Figure 7**) (25, 32), it is possible that observed correlation reductions in SCZ could be merely reduced by elevations in unshared noise. This could occur mathematically even in a setting of genuinely elevated signal-sharing, if concurrent elevations in unshared noise sufficiently exceed elevations in signal covariance.

Therefore, current clinical findings showing hyper-connectivity (when using covariance) can be reconciled with previous work suggesting hypo-connectivity (when using correlations) by considering findings in context of preferentially elevated signal variance in association regions (see **Figure 7**). These elevations in signal variance, which could involve increases in both shared and unshared variance components, could potentially reduce the absolute magnitude of connectivity measured using correlation in association regions. Put differently, although one may expect hyper-correlation in the context of elevated covariance, concurrently increased variance (potentially from an increase in the unshared variance component) may be sufficient to attenuate the measured correlation change to the point of reversing its direction (i.e. showing hypo-connectivity). Clinically, this may occur even when the absolute amount of signal shared across regions is elevated (i.e. when putative neuronal communication is increased). Therefore, it can be useful to separately quantify the absolute shared signal and the total signal variance in order to explore biophysical mechanisms that could impact each measure differently in clinical populations (e.g. long-range "global" coupling versus "local" noise amplitude).

One important question raised by present results is whether the model makes strong directional predictions of within-network findings for SCZ. The directionality of within-network connectivity changes (elevated vs. reduced) in SCZ fundamentally relates to the absolute vs. relative amount of signal shared between functionally connected regions. More specifically, measuring correlation between two signals provides a relative measure, as noted above. That is, the total signal shared is normalized by the total amount of signal variance produced by those two regions. In other words, correlations between two signals are a reflection of individual shared signal components and the "noisiness" of the remaining signal. As a result, if a third region were to send unique excitatory activity to one of the original two regions, the computed correlation between the original two regions would be reduced. This is mathematically true due to an increased unshared "noise" component in one of the original two regions. This is because of the contribution of the third region's unique signal to one of the original two regions. Therefore, if one is interested in measuring true changes in total signal shared between two hypothetical regions in the above case, then a correlation would not be the appropriate statistical metric. Put simply, a correlation would normalize the estimate of statistical dependence and is therefore impacted by new unique sources of variance (i.e. the third region in our example), regardless of whether the two original signal sources have changed. The choice to measure absolute signal shared, or alternatively relative signal shared, will impact directionality of findings in important ways.

That said, it is important to emphasize that our study is not explicitly designed to provide recommendations as to which methodology should be used to estimate functional connectivity in SCZ. As articulated above, this largely depends on whether an investigator is interested in absolute vs. relative

measures of connectivity. However, in clinical conditions where whole-brain BOLD signal variance is differentially affected relative to the control group (e.g. as was shown in SCZ, (25)), relative measures such as correlations may be problematic and may reveal 'hypo-connectivity' when in fact the shared signal (covariance) is actually elevated.

Here it is important to consider the computational modeling predictions. Specifically, the model predicts that within-network absolute connectivity will be elevated in association regions, as seen in simulations showing elevated covariance. However, the model also generates a more complex prediction that any increased within-network correlations, which increase due increased covariance, will be attenuated by concurrent elevations in unshared signal (i.e. noise). This is particularly evident from our simulations of elevated E/I ratio resulting in elevated BOLD signal variance. This will mathematically reduce the final computed functional correlation connectivity measures. In that sense, both hyper- and hypo-connectivity can be elegantly reconciled in this computational modeling framework. Put simply, studies that use correlations may observe more evidence for 'hypo-connectivity' that actually reflects elevations in variance, which overpower the effect of elevations in covariance. In turn, studies that utilize non-normalized association measures (e.g. covariance) may be more sensitive to absolute elevations in shared signal and thus would be more likely to observe 'hyper-connectivity'. It will be critical for future work in this area to carefully disambiguate which 'hypo-connectivity' effects actually arise from true shared signal reductions as opposed to elevated variance, as illustrated by our prior work (25).

Another important question raised by these effects relates to whether the model predictions can be reconciled with the existing SCZ literature. First, the literature frequently uses correlation-based connectivity measures. In turn, the model's conditional prediction with respect to correlation connectivity is that it will be reduced in association cortex under elevated E/I ratio, if and only if increases in variance sufficiently exceed increases in covariance. Therefore, as noted above, the model's predictions can be readily reconciled with the existing literature if the reduced within-network correlation connectivity in association regions in SCZ co-occurs with sufficiently severe elevations in BOLD signal variance in these same areas. As noted, it would be both important and interesting to re-examine the functional data from these studies to empirically test model predictions of elevated variance potentially masking an increase in absolute connectivity by reducing relative connectivity.

Considerations for Using Global Brain Connectivity (GBC). There are a number of methods to quantify statistical dependence between BOLD signals across sets of brain regions. As noted, above, here we used a data-driven GBC metric. Broadly, GBC is the arithmetic mean of connectivity between one brain region and the rest. Specifically, we used covariance as our connectivity measure when computing GBC in this study. However, there exist situations wherein GBC (using covariance) may not be ideal. For example, suppose that there are two profoundly anti-correlated modes that characterize resting state fluctuations. This means that half the voxels or regions will show positive covariances (within each mode) and the other half will show negative covariances (between each mode). In this situation, the mean covariance will be (nearly) zero. GBC metrics may therefore be a poor measure of functional connectivity under this circumstance. In order to avoid this scenario, some studies employ principal component analysis, and related approaches, to assess functional connectivity instead (48). However, we qualify the use of the GBC metric in the context of the current study by outlining the following rationale:

First, present findings of concern comparisons of group-level differences in GBC for SCZ patients vs. healthy subjects. Although it is possible that patients and healthy subjects could differ on some additional functional connectivity aspect that is not captured by GBC, the aim of this study was, at the most basic level, to demonstrate group differences on a measurable effect that is predicted by our model. Critically, the model is fully capable of generating predictions on any number of additional resting-state functional neuroimaging measures beyond GBC and variance, to be compared with empirical data. Future computational psychiatry studies may improve upon these findings by assessing additional functional connectivity measures following this combined computational modeling and clinical neuroimaging framework.

Second, it is important to highlight that precisely for reasons such as the scenario outlined above, we evaluated model results without removal of the global signal from the data, which would induce more anti-correlations mathematically. Critically, without global signal removal (GSR), there are far fewer instances

wherein the above scenario would actually apply. Put differently, prior to GSR more of the functional connectivity values will be in the positive range since GSR effectively 'de-means' the data or 'zero-centers' the data. For this reason, when using a GBC-type metric without GSR, the average of connection values will rarely yield a zero solution in a highly connected region, such as the fronto-parietal network (which is where most of our findings are centered on). That said, future work should consider de-composing the values into positive and negative ranges using more sophisticated implementations of GBC to verify the generalizability of this effect.

Third, the GBC metric, despite some limitations, is effectively a 'data-driven' summary of a given node's connectivity, which has practical implications. As mentioned, GBC is a measure that examines connectivity from a given voxel (or area) to all other voxels (or areas) simultaneously by computing average connectivity strength – thereby producing an unbiased approach as to the location of dysconnectivity. Unlike typical seed-based approaches, if a given area is perturbed in its functional or structural connectivity consistently, irrespective of the target location, GBC remains sensitive to this alteration. Further, unlike typical seed approaches, GBC involves one statistical test per voxel (or ROI) rather than one test per voxel-to-voxel pairing, substantially reducing multiple comparisons (e.g., 30,000 rather than ~450 million tests). These improvements can dramatically increase the chances of identifying true group differences in connectivity, or individual differences correlated with behavioral symptoms, as we demonstrated for chronic SCZ and psychotic bipolar illness (3, 16, 29, 30). The use of a 'data-driven' metric here is perhaps the only valid way to evaluate the initial starting prediction of the model—because anything more specific (e.g. 'seeding' a given node) would involve further assumptions, which would additionally complicate interpretations. Similarly, the key prediction of the model was 'agnostic' as to the specific location of the disruption. That is, the study was designed to test, in a fully data-driven way, whether the model prediction holds and if so where this effect may occur. The GBC metric provided a method to test this question.

Computational Modeling Considerations. Overall, there are two key areas in our modeling approach that merit further discussion here: (1) limitations of the current model with associated considerations, and (2) important future directions for modeling work.

Considering the Impact of Diffusion-Weighted Imaging (DWI) Gyral Bias in the Model. One important issue to consider, when interpreting the DWI structural connectivity matrix we used, is the gyral bias effect. In brief, structural connectivity matrices are typically obtained based on estimates of the probability that a white matter streamline terminates in a specific location, based on diffusion weighted imaging data. There is a tendency for DWI methods to overestimate the likelihood of a white matter streamline terminating along gyral crowns. In contrast, these methods underestimate the likelihood of a white matter streamline terminating in the gyral fundus. This results in gyral bias (49), which could impact area-specific structural connectivity 'strengths'. This problem is largely mitigated in the current modeling implementation. This is because the model uses a relatively coarse parcellation of 66 cortical areas. Consequently, each model node on average corresponds to a large cortical region encompassing both gyri and sulci. It is therefore highly unlikely that any node in the model maps onto an area that exclusively shows gyral bias. That said, future modeling studies using structural connectivity matrices of higher spatial resolution may be more susceptible to gyral bias issues in certain areas.

Limitations. We have made several assumptions in order to simplify our simulations of whole-brain activity. It is worth discussing some of these assumptions, especially where they may deviate from biological realism. Specifically, we have assumed homogeneous intrinsic and extrinsic coupling, that extrinsic (between-node) coupling is completely symmetric, and that hemodynamic parameters at each node are the same. Finally, we have made assumptions about the spectral density and auto-correlation structure of endogenous noise. Noise in our model was Gaussian white noise, without the autocorrelation structure typical of more biological noise. In addition, one feature of the model simulations in Figure 4 is that baseline ('healthy regime') covariance is much higher within association cortex, as compared with sensory cortex, in the differentiated model. This is a feature that does not necessarily match biology. Figure 5E-F in contrast shows that mean sensory network covariance is actually higher than mean association network covariance in healthy subjects. In this respect, we do not seek to make any claims about what baseline connectivity of sensory vs. association networks should be, since our model is not equipped to make predictions about this aspect of neurobiology. In

Figure 4, our aim was to demonstrate that association networks are more vulnerable than sensory networks, when challenged with increasing disinhibition under the functionally differentiated model regime. In summary, there are several aspects wherein our simplified model may lack biological realism because of its underlying assumptions. In this sense, the model has been validated (by this and previous studies) in its ability to capture key macro-scale neuroimaging features via comparisons to empirical data (6, 25, 36) as opposed to comprehensive biological realism for across-network features.

However, a 'truly' validated model would arguably demonstrate more comprehensive biological realism. Indeed, some smaller-scale (4-node) models of resting-state activity already move beyond the assumption of symmetric between-node coupling (50). Toward that end, future studies should ideally improve toward more biological realism by formally validating models of whole-brain activity with respect to the assumptions outlined above.

That said, it is worthwhile to reference an influential 1988 discussion of theoretical neuroscience by Sejnowski et al., where they highlight that "Because even the most successful realistic brain models may fail to reveal the function of the tissue, computational neuroscience needs to develop simplifying models that capture important principles (51)." In that respect, the present study advances such a simplifying model, which has been validated in its ability to capture key macro-scale neuroimaging features via comparisons to empirical data by Deco and colleagues as well as by our own group in 2014 (6, 25, 36). Outstanding assumptions notwithstanding, the key utility of the presented modeling framework is its ability to explicitly generate a key insight regarding the observed disruptions in SCZ – a prediction which was tested empirically in this study by measuring BOLD signal variance and functional connectivity in SCZ patients and matched healthy subjects.

Future Directions. As mentioned in the main text, the study used a cortical model, which does not include subcortical structures. Therefore, the model in its current form is inherently limited in its ability to make predictions about hypotheses that rely upon subcortical sources of neural disturbance, including subcortical dopaminergic projections. Incorporation of subcortical structures and accompanying 'functional neurotransmitter loops' (e.g. the dopamine pathways) will be an important direction of expansion for future studies. More broadly, the current model predominately simulates the effects of glutamate and GABA in local cortical microcircuits, without explicitly modeling effects of other 'ascending' neurotransmitters, such as dopamine. Future studies may improve upon present findings by explicitly integrating the effects of additional neurotransmitters—particularly those implicated in 'focal' hypotheses of SCZ (e.g. region-specific disruptions in dopaminergic projections), as a competing model to the global disturbance model we used in this study.

SI REFERENCES

1. Andreasen NC, Pressler M, Nopoulos P, Miller D, & Ho B-C (2010) Antipsychotic dose equivalents and dose-years: a standardized method for comparing exposure to different drugs. *Biol. Psychiatry* 67(3):255-262.

2. Anticevic A, Repovs G, & Barch DM (2012) Emotion Effects on Attention, Amygdala Activation, and Functional Connectivity in Schizophrenia. *Schizophr. Bull.* 38(5):967-980.

3. Anticevic A*, et al.* (2012) Global Prefrontal and Fronto-amygdala Dysconnectivity in Bipolar I Disorder with Psychosis History. *Biol. Psychiatry* 73(6):565-573.

4. Power JD*, et al.* (2011) Functional network organization of the human brain. *Neuron* 72(4):665-678.

5. Van Essen DC (2005) A Population-Average, Landmark- and Surface-based (PALS) atlas of human cerebral cortex. *Neuroimage* 28(3):635-662.

6. Deco G*, et al.* (2013) Resting-State Functional Connectivity Emerges from Structurally and Dynamically Shaped Slow Linear Fluctuations. *J. Neurosci.* 33(27):11239-11252.

7. Hagmann P*, et al.* (2008) Mapping the structural core of human cerebral cortex. *PLoS Biol.* 6(7):e159.

8. Anticevic A*, et al.* (2014) Mediodorsal and Visual Thalamic Connectivity Differ in Schizophrenia and Bipolar Disorder With and Without Psychosis History. *Schizophr. Bull.*

9. Anticevic A*, et al.* (2014) Characterizing thalamo-cortical disturbances in schizophrenia and bipolar illness. *Cereb. Cortex* 24(12):3116-3130.

10. First MB, Spitzer RL, Miriam G, & Williams JBW (2002) *Structured clinical interview for DSM-IV-TR Axis I Disorders, Research Version, Non-patient Edition (SCID-I/NP)* (Biometrics Research, New York State Psychiatric Institute, New York).

11. Spreen O & Strauss E (1998) *A compendium of neuropsychological tests: Administration, norms, and commentary* (Oxford University Press, New York) 2nd Ed.

12. Lezak MD (1995) *Neuropsychological Assessment* (Oxford University Press, New York) 3rd Ed.

13. Barch DM & Ceaser A (2012) Cognition in schizophrenia: core psychological and neural mechanisms. *Trends In Cognitive Sciences* 16(1):27-34.

14. Krystal JH*, et al.* (2006) The vulnerability to alcohol and substance abuse in individuals diagnosed with schizophrenia. *Neurotox. Res.* 10:235-252.

15. Anticevic A, Repovs G, Corlett PR, & Barch DM (2011) Negative and Non-emotional Interference with Visual Working Memory in Schizophrenia. *Biol. Psychiatry* 70(12):1159-1168.

16. Cole MW, Anticevic A, Repovs G, & Barch DM (2011) Variable global dysconnectivity and individual differences in schizophrenia. *Biol. Psychiatry* 70(1):43-50.

17. Glahn DC, Bearden CE, Bowden CL, & Soares JC (2006) Reduced educational attainment in bipolar disorder. *J. Affect. Disord.* 92:309–312.

18. Kay SR, Fiszbein A, & Opler LA (1987) The positive and negative syndrome scale (PANSS) for schizophrenia. *Schizophr. Bull.* 13:261-276.

19. Hanlon FM*, et al.* (2011) Bilateral hippocampal dysfunction in schizophrenia. *Neuroimage* 58(1158-1168).

20. Mayer AR*, et al.* (2012) Functional imaging of the hemodynamic sensory gating response in schizophrenia. *Hum. Brain Mapp.* 34(9):2302-2312.

21. Stephen JM*, et al.* (2013) Using joint ICA to link function and structure using MEG and DTI in schizophrenia. *Neuroimage* 83:418-430.

22. Power JD, Barnes KA, Snyder AZ, Schlaggar BL, & Petersen SE (2012) Spurious but systematic correlations in functional connectivity MRI networks arise from subject motion. *Neuroimage* 59(3):2142-2154.

23. Power JD, Barnes KA, Snyder AZ, Schlaggar BL, & Petersen SE (2012) Steps toward optimizing motion artifact removal in functional connectivity MRI; a reply to Carp. *Neuroimage* 76:439-441.

24. Anticevic A*, et al.* (2012) NMDA Receptor Function in Large-Scale Anti-Correlated Neural Systems with Implications for Cognition and Schizophrenia. *Proceedings of the National Academy of Science U.S.A.* 109(41):16720-16725.

25. Yang GJ*, et al.* (2014) Altered global brain signal in schizophrenia. *Proc. Natl. Acad. Sci. U. S. A.*

26. Biswal BB*, et al.* (2010) Toward discovery science of human brain function. *Proc Natl Acad Sci USA* 107(10):4734-4739.

27. Fischl B, Salat DH, Busa E, Albert M, & Dieterich M (2002) Whole Brain Segmentation Automated Labeling of Neuroanatomical Structures in the Human Brain. *Neuron* 33(3):341-355.

28. Repovs G, Csernansky JG, & Barch DM (2011) Brain network connectivity in individuals with schizophrenia and their siblings. *Biol. Psychiatry* 15(69):967-973.

29. Cole MW, Pathak S, & Schneider W (2010) Identifying the brain's most globally connected regions. *Neuroimage* 49(4):3132-3148.

30. Cole MW, Yarkoni T, Repovs G, Anticevic A, & Braver TS (2012) Global connectivity of prefrontal cortex predicts cognitive control and intelligence. *J. Neurosci.* 32(26):8988-8999.

31. Hayes WL (1994) *Statistics* (Cengage Learning, New York, NY) 5th Ed p 1112.

32. Hahamy A*, et al.* (2014) Save the global: global signal connectivity as a tool for studying clinical populations with functional magnetic resonance imaging. *Brain Connect* 4(6):395-403.

33. Nichols TE & Holmes AP (2002) Nonparametric Permutation Tests for Functional Neuroimaging: A Primer with Examples. *Hum. Brain Mapp.* 15:1-25.

34. Saad ZS*, et al.* (2012) Trouble at rest: how correlation patterns and group differences become distorted after global signal regression. *Brain Connectivity* 2(1):25-32.

35. Fox MD*, et al.* (2005) The human brain is intrinsically organized into dynamic, anticorrelated functional networks. *Proc Natl Acad Sci USA* 102(27):9673-9678.

36. Deco G*, et al.* (2014) How local excitation-inhibition ratio impacts the whole brain dynamics. *J. Neurosci.* 34(23):7886-7898.

37. Wong KF & Wang XJ (2006) A recurrent network mechanism of time integration in perceptual decisions. *J. Neurosci.* 26(4):1314-1328.

38. Felleman DJ & Van Essen DC (1991) Distributed hierarchical processing in the primate cerebral cortex. *Cereb. Cortex* 1(1):1-47.

39. Murray JD*, et al.* (2014) A hierarchy of intrinsic timescales across primate cortex. *Nat. Neurosci.* 17(12):1661-1663.

40. Meyer-Lindenberg A*, et al.* (2001) Evidence for abnormal cortical functional connectivity during working memory in schizophrenia. *Am. J. Psychiatry* 158(11):1809 –1817.

41. Garrity AG*, et al.* (2007) Aberrant "default mode" functional connectivity in schizophrenia. *The American journal of psychiatry* 164(3):450-457.

42. Whitfield-Gabrieli S*, et al.* (2009) Hyperactivity and hyperconnectivity of the default network in schizophrenia and in first-degree relatives of persons with schizophrenia. *Proc Natl Acad Sci USA* 106(4):1279–1284.

43. Chai XJ*, et al.* (2011) Abnormal medial prefrontal cortex resting-state connectivity in bipolar disorder and schizophrenia. *Neuropsychopharmacology* 36(10):2009-2017.

44. Hoffman RE, Fernandez T, Pittman B, & Hampson M (2011) Elevated functional connectivity along a corticostriatal loop and the mechanism of auditory/verbal hallucinations in patients with schizophrenia. *Biol. Psychiatry* 69(5):407-414.

45. Woodward ND, Karbasforoushan H, & Heckers S (2012) Thalamocortical dysconnectivity in schizophrenia. *Am. J. Psychiatry* 169(10):1092-1099.

46. Friston KJ (2011) Functional and effective connectivity: a review. *Brain Connectivity* 1(1):13-36.

47. Cole MW, Yang GJ, Murray JD, Repovs G, & Anticevic A (In Press) Functional connectivity change as shared signal dynamics. *Journal of Neuroscience Methods*.

48. Friston KJ (1996) Theoretical neurobiology and schizophrenia. *Br. Med. Bull.* 52(3):644-655.

49. DC VE*, et al.* (2013) Mapping Connections in Humans and Non-Human Primates: Aspirations and Challenges for Diffusion Imaging. *Diffusion MRI: From Quantitative Measurement to In vivo Neuroanatomy*, eds H J-B & TE B (Academic Press), 2, revised Ed, pp 338-354.

50. Kahan J*, et al.* (2014) Resting state functional MRI in Parkinson's disease: the impact of deep brain stimulation on 'effective' connectivity. *Brain* 137(Pt 4):1130-1144.

51. Sejnowski TJ, Koch C, & Churchland PS (1988) Computational neuroscience. *Science* 241(4871):1299-1306.